www.amlett.com, www.vbripress.com/aml, DOI: 10.5185/amlett.2014.amwc.1030 Published online by the VBRI press in 2014

Thermodynamics and electrochemical characterization of core-shell type gold–coated superparamagnetic iron oxide nanoparticles

Faruq Mohammad[1,2], Tanvir Arfin[3]*

[1]*Institute of Advanced Technology, Universiti Putra, Serdang, 43300 Selangor, Malaysia*
[2]*Department of Environmental Toxicology, Southern University and A&M College, Baton Rouge, LA 70813, USA*
[3]*Department of Chemistry, Uka Tarsadia University, Maliba Campus, Gopal Vidyanagar, Bardoli 394350, India*

*Corresponding author. Tel: (+91) 7878366678; E-mail: tanvirarfin@ymail.com

Received: 26 August 2013, Revised: 18 October 2013 and Accepted: 25 October 2013

ABSTRACT

In continuation to our previous work, the superparamagnetic Fe_3O_4@Au core-shell type nanoparticles (NPs) were further characterized by differential scanning calorimetry (DSC), thermogravimetric analysis (TGA), electrical conductivity, impedance and cyclic voltammetry measurements. From the analysis of DSC and TGA results with our Fe_3O_4@Au NPs of about 6.25 ± 0.6 nm size, we observed a clear endothermic peak at 310°C due to the decomposition of the oleic acid/oleylamine surface ligands and the particles found to contain more than 80% of the metallic content from the mixed compositions of gold and iron oxide. Because of the conduction through the Fe_3O_4@Au grain, the impedance profile of the pellet exhibited a well-resolved semi-circle and an inclined spike in a far low-frequency region. The electrical conductivity of the Fe_3O_4@Au material found to be increased with an increase of temperature. The standard Gibbs free energy (ΔG) of the reaction provided a criterion for spontaneous changes in the equilibrium of the material. From the analysis of the results of ΔG, it appears that at 25°C temperature, ΔS found to be negative. The calculated enthalpy, ΔH = -0.635 kJ/mol, at the corresponding entropy of ΔS = -0.132 kJ/mol. Finally, the activation energy in temperature range of 25-200°C for the Fe_3O_4@Au core-shell material was calculated using Line fitting and the surface characterization by using cyclic voltammetry. The electrochemical redox property of the Fe_3O_4@Au quasi-reversible wave corresponding to Au^{3+}/Au^{2+}. In addition, the electrochemical parameters for Fe_3O_4@Au NPs of $(E_p^c), (E_p^a), (E_{1/2}^0)$ and ΔE were also obtained. Since the Fe_3O_4@Au material has low activation energy at low temperature range which makes it a good candidate as an ion conductor and even has the potential uses in many solid state devices and also in the future prospects of electrochemistry applications. Copyright © 2014 VBRI press.

Keywords: Fe_3O_4@Au; gold nanoshell; Core-shell structure; electrical conductivity; impedance measurements; Gibbs free energy; activation energy.

Faruq Mohammad obtained his Ph.D. from the Department of Environ mental Toxicology, Southern University and A&M College (Baton Rouge, LA, USA) in May 2011. Prior to this, in 2005, Mohammad obtained his Master's degree in Synthetic Organic Chemistry from Acharya Nagarjuna University (Namburu, India). He is currently working as the post-doc research fellow in the Institute of Advanced Technology, Universiti Putra Malaysia. His area of research is in the development of polymeric nano drug delivery systems for malaria and cancerous diseases, biomedical applications of metal nanomaterials, in addition to understanding the nanoparticles toxicity. He has several publications in these areas.

Tanvir Arfin is currently working as an assistant professor in the Department of Chemistry, Uka Tarsadia University, India. He has received his Master degree in Physical Chemistry and Ph.D. in Membrane Electrochemistry from the Aligarh Muslim University in India. After obtaining the Ph.D. degree, he appointed as the post-doctoral fellow at North West University in South Africa for about 3 years. Dr. Arfin has been actively engaged in various fields of electrochemistry, PGM, polymer science, membrane, hybrid material, development of graphite oxide and understanding nanomaterials toxicity. He has published more than 18 scientific peers reviewed journal papers and 3 book chapters.

Introduction

In recent years, research into the development of multifunctional, electrically conductive and thermally stable materials has been the subject of interest, as it provides sophisticated materials for the current advancing applications of catalysis, fuel cell technology and electrochemical batteries. The exploration of materials led to the design and synthesis of nanomaterials with complex geometries such as alloy, core-shell, onion-type, multilayered, multimetallic and multifunctional nanoparticles (NPs); as the materials with these structures offer a number of useful physiochemical properties in addition to chemical and thermal stability which opens up new possibilities for their use **[1-2]**. The nanomaterials are characterized by their large surface area and there are a number of approaches by which one can bring about surface morphological changes that can lead to concomitant changes in their optical, electrochemical and thermodynamic properties. One of the ways at which the optical and electrical properties of NPs can be tailored is by making use of the bimetallic architecture, as this is often more active than the corresponding pure metal. Due to the large surface area, thermally stable and highly conductive behavior of bimetallic NPs, they can endure fast redox reactions and therefore, can serve as platforms for electrochemical devices. A number of reports have been generated in the literature whose concern is primary limited to either studies of the electrical properties or thermodynamic analysis of "alloy" type-oxide nanomaterials **[3-5]**. However, our interest is to investigate the electrochemical and thermodynamic parameters of iron oxide-coated metallic gold shell NPs, as the core-shell architecture offers greater opportunities to modulate the properties of both core as well as the shell nanomaterial. In addition, because of the presence multiple elemental compositions within a single particle, the core-shell structure offers highly stable metal oxide-metal combination through strong electrophilic attraction between the core and shell **[1]**.

Iron oxide has been referred to as the promising material for the desired application in biological, chemical, industrial areas and it exhibit large surface-to- volume ratio, high surface reaction activity, high catalytic efficiency, superparamagnetism, low toxicity, a unique ability to promote high electron transfer capability between the electrodes and high as well as strong adsorption ability that is very helpful in obtaining the improved stability and sensitivity of a sensor **[6]**. In recent year, the superparamagnetic iron oxide nanoparticles hav gained vast attention because of its application as contrasting agents for magnetic resonance imaging (MRI) **[7]**. It was also noticed that the aggregation of Fe_3O_4 nanoparticles due to high surface area and magnetic dipole interaction between nanoparticles has limited their applications **[8]**.

Gold nanoparticles has unique sensing properties due to its intriguing optical characteristic and can find applications in electronics **[9]**, photodynamic therapy **[10]**, therapeutic agent delivery **[11]**, sensors **[12]**, probes **[13]**, diagnostics **[14]** and catalysis **[15]**. It also exhibits the property of surface plasmon resonance (SPR) **[16]**. This SPR property of gold nanoparticles can be useful in other areas such as in vitro assays, in vitro and in vivo imaging, cancer therapy, and drug delivery **[17]**.

The thermodynamic properties are endorsed which is generated by the absolute rate of interaction between particles. This is represented as a ability to show transition from initial to final state leading to one intermediate state that is very common as activated complex which correspond to the peak of the curve of potential energy. The above statement is referred according to the Eyring theory **[18]**. The maximum height of the peak is distinguishing the initial and final stable state which is characterized by minimal potential energy. Based on this theory itself, the calculation of the thermodynamic characteristics of ion migration is done and namely through, the changing of Gibbs energy ΔG, entropy ΔS and enthalpy ΔH of reacting substances in their normal standard state **[18]**.

Generally the electrical properties of the conducting materials (in our case, Fe and Au) accompanied by changes in dimension, conductivity or permittivity can be easily measured by electrical impedance techniques, as it requires only the application of two or more electrodes. The impedance spectroscopy became a powerful analytical tool for the analysis of electrochemical phenomena concerning the solid state, porous materials and its unique ability resolves the electrical responses of individual components in complicated systems **[19, 20]**. In particular, the non-steady technique AC impedance spectroscopy is suitable to investigate the complex electrochemical systems and this technique can separate the phenomena with different relaxation times and is also useful for the determination of rate limiting step occurring at the electrode surfaces **[21]**. AC conductivity is one of the frequent investigating approaches applied on solids for characterization of the bulk resistance present in the material sample which has been allowed for the measurement of the electrical properties. Different technique has been performed for the measurement of AC conductivity. The complex impedance spectroscopy is unique and currently as well as sparsely used advanced technique. The measurement technique of AC conductivity gives brief information regarding the electrical properties of material along with the interface of electronically conducting electrodes **[22]**.

The direct oxidation or reduction of substrate detects the electrochemical methods acting on the electrode surface. Electrode reactions are very appreciable and suitable for the analytical applications because of its high potential requirements **[23]**. The most common method that is electrochemical determination has been here regarded as fastest, cheapest and long lasting technique in the analytical quantitative determination of different analytical species **[24]**. Cyclic voltammetry is also one of the most versatile electroanalytical techniques for the study of electroactive species, as it observes the rapid changes in redox behaviours over a wide range of potentials and electrolyte solutions. The cyclic voltammogram is a display of current versus potential and the procedure involves the measuring of current at the working electrode during each potential scan **[25]**.

We previously demonstrated that the superparamagnetic iron oxide nanoparticles on coating with gold (Fe_3O_4@Au) enhance the heat releasing properties up to five fold as compared with the bare Fe_3O_4 NPs of the similar type **[1]**. We also observed changes in the magnetic properties and blocking temperatures of Fe_3O_4@Au NPs when bound to cysteamine and further to protein such as luteinizing hormone-releasing hormone **[2]**. The synthesis and characterization of Fe_3O_4@Au nanoparticles have aimed at many areas for potential applications. Our studies have focused on the electrochemical and thermodynamical properties of the interfacial reactions, as the gold shell provides an intrinsic as well as devastating platform for assessing the core@shell nanostructures.The Fe_3O_4@Au core-shell imparts the superparamagnetic nanoparticles with many intrinsic functional properties. Further, in this report we extended our understanding on the core-shell type Fe_3O_4@Au NPs with the studies of impedance measurements, temperature dependent electrical conductivity, thermodynamic parameters of Gibbs free energy and also with the cyclic voltammetry. To the best of our knowledge, this is the first report concerning the thermodynamic behaviour and cyclic voltammetry of metal oxide@metal core-shell type NPs and their electrical conductivity measurements. The reason for conducting these studying is to understand how different microstructures would influence the electrochemistry of gold containing architectures. Since during recent years, the gold-supported metal oxides have been advancing due to their potential applications as ionic conductors, active catalyst materials, optical detection and imaging platforms, electrochemical-signal detection based amperometric nanobiosensors. There are many other potential applications which are part of our on-going work and the results will be discussed in our future reports.

Experimental

Materials

Iron acetylacetonate (≥ 99.9%), diphenyl ether (≥ 99%), oleic acid (≥ 99%), oleylamine (70%), 1,2 hexadecanediol (90%), hexane (≥ 97%) and ethanol(≥ 99.8%), were purchased from Sigma-Aldrich (USA) and used as supplied. Gold acetate (99.9%) was obtained from Alfa-Aesar (USA) and all chemicals received were of analytical grade and were without any further purification later on before experimentation. Ultra-pure water of resistivity 18.2 MΩcm was obtained from a Milli-Q water purification system (Millipore Corp., Bedford, MA, USA).

Synthesis of Fe_3O_4 NPs

In order to obtain the core-shell NPs of iron oxide-coated gold, we followed the procedure as described by Mohammad *et al* **[1]**. Briefly, 0.7 g of iron acetylacetonate was mixed with a solution containing 20 mL of diphenyl ether, 2 mL of oleic acid, and 2 mL of oleylamine under inert atmosphere with vigorous stirring in a three-necked round bottom flask. To this solution, 2.6 g of 1,2-hexadecanediol as reducing agent was added. Now the reaction mixture was heated to around 210°C with reflux for 2 h and maintained the oxygen-free conditions throughout the reaction period. The reaction mixture was cooled to room temperature, and then, degassed ethanol was added to precipitate the black-colored product of iron oxide NPs. The precipitate was separated out by centrifugation (Eppendorf 5424 microcentrifuge, USA) at 1500 rpm/min for 15 min, washed with a series of solvents starting with hexane, followed by a mixture of hexane and ethanol, and then finally with ethanol. The product was dispersed in ethanol, separated out magnetically and dried to obtain black powder of iron oxide NPs.

Synthesis of Fe_3O_4@Au NPs

In the following step, to 10 mL of diphenyl ether, approximately 0.5 g of previously prepared iron oxide NPs was added. Further to this mixture, a solution containing 30 mL of diphenyl ether, 3.1 g of 1,2-hexadecanediol, 0.5 mL of oleic acid, 3 mL of oleylamine, and 0.8 g of gold acetate was added under inert atmosphere. The reaction mixture was heated to around 190°C with reflux for about 1.5 h. After the mixture was cooled to room temperature, ethanol was added, and the dark purple material was separated out by centrifugation at 3000 rpm/min for 15 min. The material was re-suspended in hexane, washed 3-5 times with ethanol, and dried under inert atmosphere. By suspending the particles in ethanol, the gold-coated iron oxide NPs were separated using magnetic separation technique.

Instrumental characterization of Fe_3O_4@Au NPs

High resolution transmission electron microscopy (HRTEM) measurements were carried out on JEOL-2010 HRTEM instrument with a point to point resolution of 1.94 Å, operated at a 200 kV accelerating voltage. The HRTEM samples were prepared by taking a droplet of Fe_3O_4@Au NPs in hexane onto a carbon coated copper grid and evaporating the solvent at room temperature.The FT-IR spectra were obtained using Nexus 670 FT-IR spectrometer in the transmission mode in the range of 4000-400 cm^{-1} and the samples were prepared by finely grinding the compound with dry KBr powder and then made into a transparent pellet. For thermogravimetric analysis (TGA), the sample was heated upto 600°C at a rate of 10°C per min on a TA 600 instrument and the sample was held at the final elevated temperature for 10 minutes to ensure complete removal of all volatile materials. Powdered X-ray diffraction (XRD) patterns were recorded on a Bruker-Siemens D5000 automated powder diffractometer using Cu-Kα radiation and the data were collected from 20-80° units in 2θ (theta) at a scan rate of 0.06° per step. The Perkin Elmer instrument was employed to record differential scanning calorimeter (DSC) curve for the material in nitrogen atmosphere with a flow rate of 10mL/min over a temperature range of up to 550°C and a heating rate of 10°C/min was applied. The α-Alumina was used as a reference material and for the analysis; around 10-15 mg of sample was placed in α-Alumina crucible. The electrical conductivity and impedance measurements were performed by using a high tester HIOKI-3532 50 LCR METER in the frequency range 42Hz-5MHz. The powdered samples of Fe_3O_4@Au were compressed at 10

MPa to form pellets, further coated with carbon black paint and annealed between the electrodes for two hours at 120ºC to enhance the electrical connectivity between Fe_3O_4@Au and the electrodes. The cyclic voltammograms were recorded on a CH-Instrument Electro-Chemical Analyzer using tetraethylammonium perchlorate as a supporting electrolyte at room temperature. A three cell electrode is used which contains a Pt micro cylinder working electrode, Pt wire as auxillary electrode and Ag/AgCl as the reference electrode. All electrochemical data were collected at 25°C and are uncorrected for junction potentials. The voltammograms were generated through computer stimulation giving the magnitudes of reduction, oxidation and half-wave potentials of the redox processes. All the experiments were conducted at room temperature and were repeated at least three times to check the reproducibility. Non-linear regression analysis (NLR) fits were performed using Origin® software (version 8, OriginLab Corporation).

Results and discussion

High-Resolution transmission electron microscopy (HRTEM) studies of Fe_3O_4@Au NPs

The Fe_3O_4@Au NPs were obtained by the thermal decomposition of organic metallics at higher temperature conditions and also in the presence of suitable reducing agent. **Fig. 1** shows the HRTEM image and size distribution of Fe_3O_4@Au NPs. As evidenced by the inter-particle space and its uniformity from the HRTEM analysis, the NPs are spherical in shape and are covered completely by the surfactants oleic acid-oleylamine forming a capping monolayer which protects them from the particle-particle interactions. Also from the size distribution analysis, the average particle size of Fe_3O_4@Au NPs obtained to be 6.25 ± 0.6 nm.

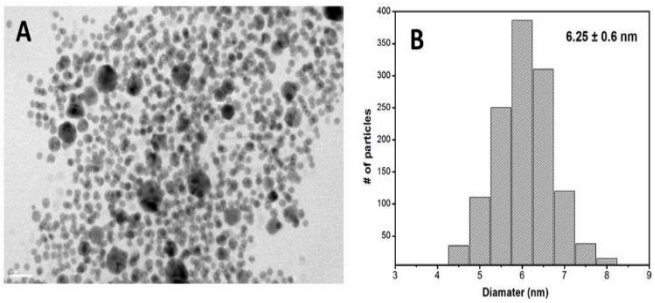

Fig. 1. HRTEM image (A) and the size distribution analysis (B) of Fe_3O_4@Au NPs (scale: 20 nm).

Fourier transform infrared spectroscopy (FTIR) studies of Fe_3O_4@Au NPs

The FT-IR spectrums were recorded to identify the surface functionality in Fe_3O_4@Au NPs and were compared with pure oleic acid, oleylamine (**Fig. 2**). From the figure, the presence of peak for (a) around 545 $cm^{-1}$is due to the split of v_1 band corresponding to the Fe-O band of magnetite and other band at 430 cm^{-1} due to the v_2 band of Fe-O bond of magnetite. Also, there is a matching of peaks of (a) with that of (b) and (c) at 2850-3000 cm^{-1} are due to the symmetric and asymmetric methylene (CH_2) stretching modes of groups present in oleic acid and oleylamine. The sharp peak in (b) at 3319 $cm^{-1}$by the free N-H stretching vibration, appeared in (a) as a broad peak at 3425 cm^{-1} due to hydrogen bonding. The peak of (c) at 1712 cm^{-1} are due to ν(C=O) which were observed for (a) at around 1708 cm^{-1} and other peak around 960 cm^{-1} are due to the =C-H bending vibrations **[26]**. Therefore, from the comparison of all the spectrums, it proves that Fe_3O_4@Au NPs possess the mixed functional groups of oleic acid and oleylamine.

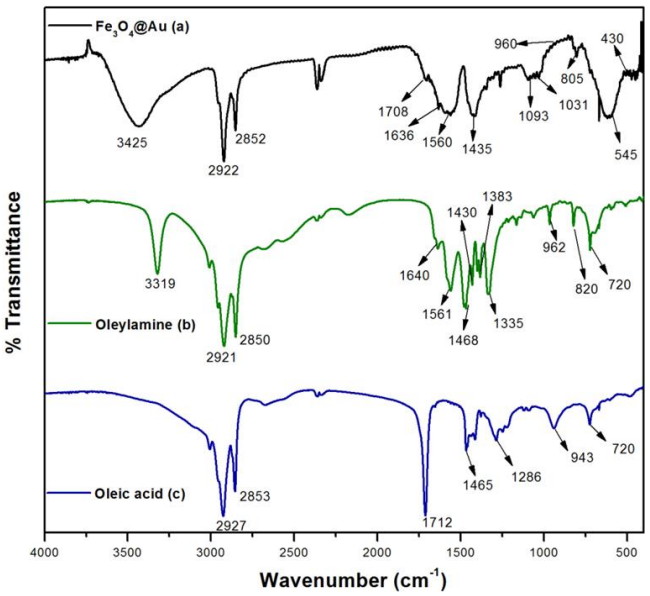

Fig. 2. Comparison of the FT-IR spectrums of Fe_3O_4@Au NPs with that of pure oleic acid and oleylamine.

Differential scanning calorimetry (DSC) and thermo gravimetric analysis (TGA) studies of Fe_3O_4@Au NPs

The DSC and TGA curves for Fe_3O_4@Au NPs in the temperature range of up to 600°C were shown in **Fig. 3**(A-B). **Fig. 3A** shows the heating mode of the DSC curve of the Fe_3O_4@Au NPs taken in temperature range of 25-550°C. From the figure, the Fe_3O_4@Au NPs show endothermic peak appeared at 310°C, which is attributed to the melting/decomposition region of the surface ligands of oleic acid and oleylamine groups. The material contains only one sharp endothermic peak and not appearance of any other peaks is an indicative of the stability of Fe_3O_4@Au up to 600°C. Further, the thermal stability of Fe_3O_4@Au NPs is illustrated by TGA study and is shown in **Fig. 3B**. The curve was fitted using degradation stages arising from thermal oxidation of the surfactant matrix of oleic acid and oleylamine. From the TGA curve of the Fe_3O_4@Au, the material shows a 5% weight loss up to 100°C temperature and this can be due to the loss of external water molecules present at the composite surface or the starting of the decomposition of oleic acid molecules. Further, a slow weight loss of about 4.0% between 100 and 273°C may be due to the slight decomposition of organic part (oleic acid/oleylamine

surfactants) of the material. Above 273°C, the presence of a smooth horizon section in the spectrum for Fe_3O_4@Au NPs demonstrates the complete conversion of the material into oxide. Therefore, from the TGA data, the Fe_3O_4@Au NPs contain a total of 82.3% of metal (i.e. 17.7% of oleic acid/oleylamine surfactants) and this weight corresponds to the mixed composition of Au and Fe_3O_4.

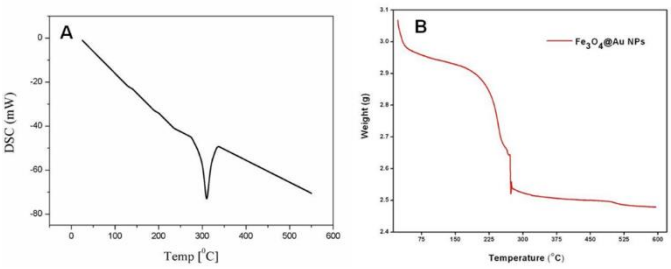

Fig. 3. DSC (A) and TGA (B) curves for Fe_3O_4@Au NPs.

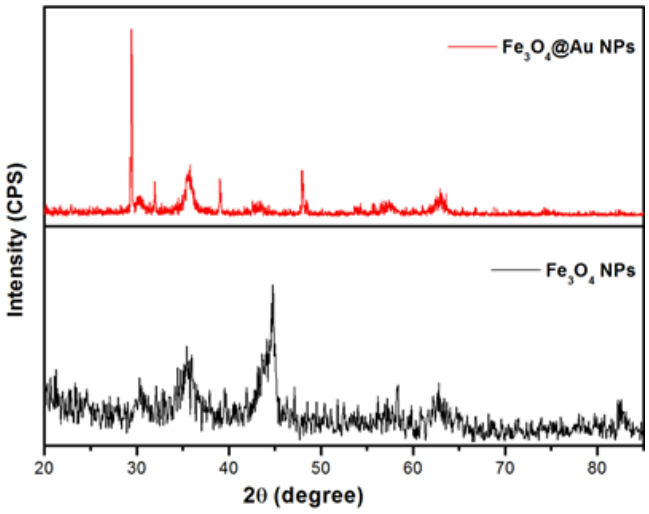

Fig. 4. Comparison of the XRD images of Fe_3O_4 and Fe_3O_4@Au NPs.

X-ray diffraction studies of Fe_3O_4@Au NPs

The powdered XRD for Fe_3O_4@Au NPs were recorded and were compared with that of Fe_3O_4 NPs and is shown in Fig.4. From the figure, the XRD of Fe_3O_4 showed the diffraction peaks at 2θ (Theta) of 30.1°, 35.1°, 42.5°, 52.7°, 56.5°, 62.1° and 70.5° **[27]**. However, for Fe_3O_4@Au NPs the diffraction peaks are at30.3°, 31.9°, 35.9, 39.6°, 44.6°, 49.5°, 58.1°, 62.9°and from the literature, the XRD peaks for the gold NPs coated with oleic acid, oleylamine were obtained to be at 39.4°, 44.1°, 51.3°, 63.8°, 76.2° **[28]**. From the analysis, the peak positions as obtained in the case of Fe_3O_4@Au NPs correspond to the planes of gold in a cubic phase. Also from the XRD pattern, no impurity peaks were detected and the Fe_3O_4@Au NPs gave the diffraction peaks similar to that of pure gold NPs and Fe_3O_4 NPs coated with oleic acid and oleylamine surface ligands. However, the absence of some of the diffraction peaks of iron oxide in Fe_3O_4@Au sample is mostly due to the heavy atom effect from gold, as a result of the formation of gold layers onto the iron oxide core. Since due to the heavy atom effect (electron configuration of gold is higher than that of iron), whatever be the x-rays falling on the outer surface of gold are getting fully absorbed/diffracted within the shell and not transmitting into the core, makes to see mostly the peaks corresponding to pure gold. The sharpness of the Bragg's reflections also indicates that the Fe_3O_4@Au NPs are nanocrystalline in nature. During the scanning, solvent scattering, the background is likely to be because of Brownian motion along with the short-range order of salvation cage all around the particles **[29]**.

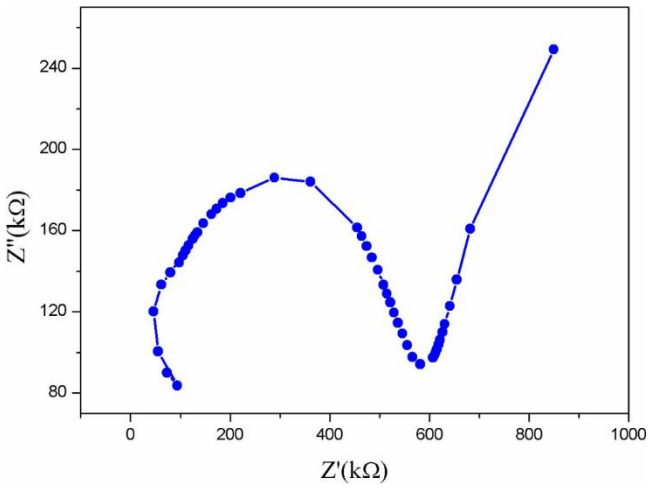

Fig. 5. Complex impedance plane plots for Fe_3O_4@Au NPs.

Impedance studies of Fe_3O_4@Au NPs

A Nyquist diagram or Cole-Cole plot can be represented in terms of any of the four possible complex formalisms, namely the impedance (Z^*), the admittance (Y^*), the permittivity (ε^*) and the electric modulus (M^*), which are connected to each other and also to the significant dielectric loss or dissipation factor ($tan\delta$) which are as follows **[30]**:

$$\frac{Z'}{Z''} = \frac{Y'}{Y''} = \frac{e''}{e'} = \frac{M''}{M'} = \tan\delta \qquad (1)$$

Fig. 5 shows the impedance complex plan plots (Nyquist plots) as obtained by plotting the imaginary part with corresponding real part at each excitation frequency. It is quite evident from the figure that the Fe_3O_4@Au sample shows a semicircle within the region of the measured frequencies and a low frequency inclined spike is also found due to the conduction of the grain. It is also observed that at high frequencies, the impedance of the Randles cell was almost entirely created by the ohmic resistance and the frequency reaches to its maximum limit at the left most end of the semicircle. It has been found that the idealized impedance plot of the material mostly consists of a semicircle attributed to the grain and the grain boundary and the low frequency inclined spike are due to the ionic polarization, electrochemical reactions which is occurring onto the electrode interface **[31, 32]**. In addition to it, the appearance of the spikes is an indication that the conduction in Fe_3O_4@Au is ionic in nature **[33]**. Impedance is regarded as an effective tool to study the

interfacial properties of the electrode modified at the surface. A Faradic impedance spectrum at Nyquist plot is including a semicircular region which is observed at higher frequency that is corresponding an electron-transfer limited process on the Z' axes which is followed by a linear straight line at 45° to the real axes at lower frequencies revealing the diffusion of limited electron transfer process **[34, 35]**. The impedance is a complex number and is defined by **[36]**

$$Z^*(\omega) = Z' + jZ'' \quad (2)$$

$$= \frac{R}{\left[1+\left(\frac{j\omega}{\omega}\right)^{1-\alpha}\right]} \quad (3)$$

$$j = \sqrt{-1} \quad (4)$$

Impedance can be separated into real and imaginary parts by algebraic rules, where j is the imaginary unit. R is the overall resistance at a frequency of ω (radian) and α is the deviation magnitude of the electrical response for an ideal condition. When α is equal to zero, the Cole-Cole model reduces the Debye model and when α is greater than zero, the relaxation is stretched. If α is equal to 0.5, it depicts the Wardburg impedance for homogeneous semi-infinite diffusion **[32]**. The electrical resistance (Z'') is the real part of the impedance and the capacitive reactance (Z') is the imaginary part of the impedance. (Z') and (Z'') are given as follows **[37]**:

$$Z' = Z\sin\theta = \frac{R_g^2\omega_g C_g}{1+\omega_g^2 C_g^2 R_g^2} \quad (5)$$

$$Z'' = Z\cos\theta = \frac{R_g}{1+\omega_g^2 C_g^2 R_g^2} \quad (6)$$

where θ is the phase angle and defined by:

$$\theta = \tan^{-1}\left(\frac{Z'}{Z''}\right) \quad (7)$$

where the resistance of grain (R_g) can be directly obtained from the intercept of the Z′-axis **[37]**. The angular frequency of grain (ω_g) is obtained at the maxima of the semicircle. As Z′ = Z″, at maximum point in the semicircle, the capacitance (C_g) can therefore be calculated according to eq. (8)

$$C_g = \frac{1}{R_g\omega_g} \quad (8)$$

The relaxation time τ_g is obtained from the angular frequency at the maxima using the relations:

$$\tau_g = \frac{1}{\omega_g} = C_g R_g \quad (9)$$

But,

$$\sigma = \frac{1}{R_g} \quad (10)$$

So we can get

$$R_g = \frac{1}{\sigma} \quad (11)$$

Substituting Eq. (11) in (9) we get,

$$\tau_g = \frac{C_g}{\sigma} \quad (12)$$

where σ denotes the conductivity and eq. (12) implies that the relaxation time is inversely proportional to conductivity in the present study. It is assumed that τ_g indicates the mean time between the two consecutive jumps of an anionic vacancy. The diffusion coefficient D is related to τ_g as follows **[38]**:

$$D \propto \frac{\gamma d^2}{\alpha\tau_g} \quad (13)$$

Alternatively, the diffusion coefficient (D) is related to τ_g as follows:

$$D \propto \frac{1}{\tau_g} \quad (14)$$

From Eq. (13), d^2 is the mean square jump distance between two adjacent anionic sites in the crystal lattice; γ and α are the correlation and geometric factor, respectively. For a two dimensional diffusion, α= 4. Since the diffusion coefficient D is inversely proportional to the relaxation time in eq. (14), meaning that for a shorter τ_g, greater will be the diffusion coefficient, leading to a high ionic conductivity. In our present system, there is only one semicircle obtained at the higher frequency region, but no semicircle is obtained at the lower frequency region, which is not recognised adequately by the any such grain boundary region. The calculated values of equivalent circuit parameters are listed in **Table 1** and this is clearly reflected by the low value of corresponding relaxation time τ_g.

Table 1. Equivalent circuit parameters estimated from the impedance spectra for Fe_3O_4@Au NPs.

R_g (kΩ)	C_g (F)	τ_g(s)
624.053	4.414×10^{-6}	2.754×10^{-3}

One specific semicircular arc which is exhibited in the impedance spectra of the material can be modulated by a series of association of one circuit. This circuit generally consist of resistor (R_g) and the capacitance (C_g) is arranged in parallel circuit ($R_g - C_g$) which is considered to be the grain interior contribution. The total resistance (R) of a material is now said to be a grain boundary resistance.

The value of the initial resistance is 73.22 (kΩ) for the Fe_3O_4@Au material. Resistance is generally frequency-independent in nature. Resistance in no sense is described by ω at all, so resistance is represented on a Nyquist plot by a single point on the Z′ (**Fig. 5**). On a Nyquist plot of Z″ against Z′, the impedance of a capacitor is represented by a vertical line along the y-axis, with its value descending on the axis as the frequency increases rapidly, going from Z′ = 0 when ω = ∞ to Z″ = ∞ at ω = 0. This feature of a pure capacitor is described as capacitive 'spike', because of the vertical nature of the line along the axis. In fact, semicircular features in Nyquist plots represent the layers that have both resistive and capacitive components, i.e. they behave as RC elements respectively. The linear part of spectrum is well fitted and depicted as a straight line whose slope is varied around the range of π/4 resembling the Warburg-type diffusion **[39]**.

Table 2. Thermodynamic parameters of Fe_3O_4@Au NPs.

E_a(kJ/mol)	ΔG(kJ/mol)	ΔS(kJ/mol)	ΔH(kJ/mol)
1.599	39.296	-0.132	-0.635

Electrical conductivity studies of Fe_3O_4@Au NPs

The temperature dependence of ionic conductivity expressed by the Arrhenius equation as **[40-44]**:

$$\sigma T = \sigma_0 \exp\left(\frac{-E_a}{\kappa T}\right) \quad (15)$$

where σ_0 is the pre-exponential factor of the conductivity, σ_0 actually depends on temperature, but less rapidly than exponentially, k is the Boltzmann constant, T the absolute temperature and E_a is the activation energy for the conductivity.

On taking log on both the sides then we get,

$$\log(\sigma T) = \log(\sigma_0) - \left(\frac{-E_a}{\kappa T}\right) \quad (16)$$

The temperature dependence of electrical conductivity for the Fe_3O_4@Au material is shown in **Fig. 6**. It shows that the conductivity was found to increase exponentially with an increase in temperature. The activation energy of material is calculated from the slope according to the Arrhenius equation using least square analysis of the experimental data (**Table 2**).

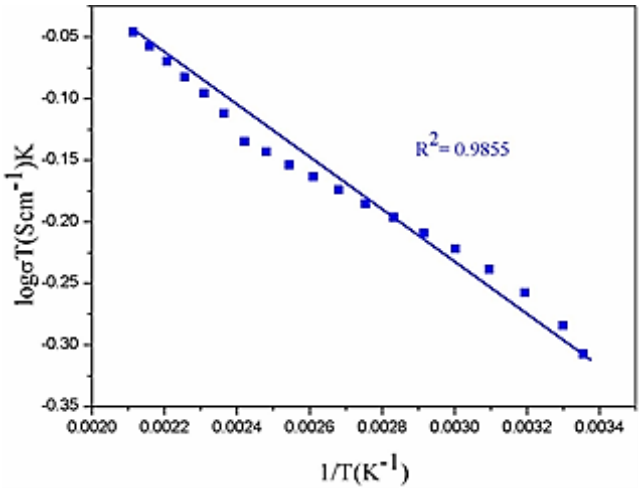

Fig. 6. Temperature dependence of electrical conductivity for Fe_3O_4@Au NPs.

The well-known Eyring equation from the theory of activated complex (transition state) can be written in the following form **[18]**:

$$\sigma = \left(\frac{RT}{Nh}\right) \exp^{-\left(\frac{\Delta G}{RT}\right)} \quad (17)$$

where h is the Planck's constant, R the gas constant, N the Avogadro's number, T the temperature in Kelvin, ΔG the free of Gibbs energy of the material.

The standard enthalpy (ΔH) and entropy ($T\Delta S$) of the material can be calculated by

$$\Delta H = \frac{\partial\left(\frac{\Delta G}{T}\right)}{\partial\left(\frac{1}{T}\right)} \quad (18)$$

$$T\Delta S = \Delta H - \Delta G \quad (19)$$

Equation (17) can be rewritten as follows [45]:

$$\sigma = \left(\frac{RT}{Nh}\right) \exp^{-\left(\frac{\Delta H}{RT}\right)} \exp^{\left(\frac{\Delta S}{R}\right)} \quad (20)$$

On taking log the expression gives,

$$\log\left(\frac{\sigma Nh}{RT}\right) = \left(\frac{\Delta S}{R}\right) - \left(\frac{\Delta H}{RT}\right) \quad (21)$$

Eq. (21) predicts a line fitting relationship between

$\log\left(\frac{\sigma Nh}{RT}\right)$ and $\left(\frac{1}{T}\right)$ in Fig.7.The values of $\left(\frac{\Delta S}{R}\right)$ and $\left(\frac{\Delta H}{R}\right)$ for the material can be evaluated from the ordinate intercept and initial slope of the plot of $\log\left(\frac{\sigma Nh}{RT}\right)$ and $\left(\frac{1}{T}\right)$.

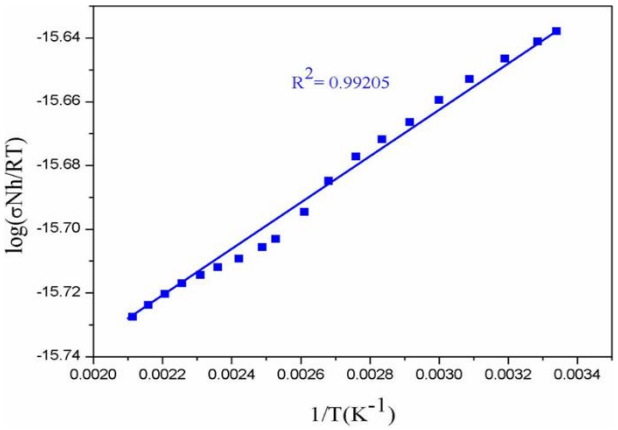

Fig. 7. Temperature dependence of log on electrical conductivity for Fe_3O_4@Au NPs.

The interacting forces within Fe_3O_4@Au exhibits weak interaction such as electrostatic forces, hydrophobic interaction, hydrogen-bond formation, Van der Waals forces and stereo-hindrance effects **[46]**. The thermodynamic parameters, enthalpy change (ΔH), entropy change (ΔS) and free energy change (ΔG) are the main evidence for confirming the binding modes. From the thermodynamic standpoint, ΔH > 0 and ΔS > 0 implies a hydrophobic interaction; ΔH < 0 and ΔS < 0 reflects van der Waals force or hydrogen bond formation; and ΔH ≈ 0 and ΔS > 0 suggests an electrostatic force. The positive ΔS value can be taken as the evidence for hydrophobic interaction. The large positive value of ΔS interprets the breaking of reflecting bonds which is indicated by mechanism of flow according to Eyring and co-worker whereas low value of ΔS indicates that without breaking of bonds the permeation has taken place **[18]**. The formation of covalent bond between the permeable species and the material is due to negative value of ΔS which also indicates that the rate determining step is not actually permeation through the material **[47]**. Furthermore, the negative ΔH value observed cannot be mainly attributed to the electrostatic interactions since for electrostatic interactions ΔH is very small, almost equals to zero. A negative ΔH value is observed whenever there is a hydrogen bond on the binding site **[48]**.

The thermodynamic parameters of Fe_3O_4@Au material are listed in Table 2. The thermodynamic parameter, ΔG found to be positive, whereas, ΔH and TΔS values are negative depending upon the nature of the material. It is not possible to account for the thermodynamic parameters of the Fe_3O_4@Au on the basis of a single intermolecular force. Consequently, the negative ΔH and ΔS values suggest the hydrophobic and hydrogen bond interactions play major roles in the Fe_3O_4@Au and contributed to the stability of the Fe_3O_4@Au. From the **Table 2**, it can also be seen that the ΔH and ΔS of Fe_3O_4@Au material are much smaller and the value of ΔS > ΔH. The positive value of ΔG reveals that the interaction process is non-spontaneous. The value of ΔG is obtained at 298K and the highest correlation coefficient R^2 (0.99205) was found just for this material.

The dependence of Gibbs free energy values with respect to temperature for the Fe_3O_4@Au material is shown in Fig.8. From the figure, it appears that ΔG is getting decreased with increase of temperature in contrast to the trends as reported by earlier investigators **[3]**. The temperature dependence of the corresponding Gibbs free energy of formation reported by different investigators suggests significantly more negative enthalpies of formation **[4, 5]**. Due to the energetically disturbed process of ion migration which lacked certain energetic barrier, the value of ΔG remains positive in nature **[44]**.

Electrochemical characterization of Fe_3O_4@Au NPs

Cyclic voltammetry is one of the most important electroanalytical techniques employed for interaction of metal complexes due to the similarity between various redox chemical processes **[49]**. To the best of authors' knowledge, no experimental result from the systematic study has been reported yet on the voltammetric behaviour Fe_3O_4@Au NPs in the redox region. The electro-chemical redox properties of Fe_3O_4@Au NPs have been studied employing cyclic voltammetry in the applied potential range +1.0 to -1.0 V recorded at 0.05, 0.1, 0.2, 0.5 and 1.0 Vs^{-1} scan rates with reference to Ag/AgCl electrode at room temperature, in presence of tetrabutylammonium perchlorates as a supporting electrolyte. The observed electro-chemical data, i.e. magnitudes of the reduction potentials $\left(E_p^c\right)$, oxidation potentials $\left(E_p^a\right)$ and half-wave potentials $\left(E_{1/2}^0\right)$ along with the representative typical cyclic voltammogram is shown in **Fig. 9**. The cyclic voltammogram for Fe_3O_4@Au NPs recorded at 0.05 Vs^{-1} scan rate exhibited a weak intensity irreversible cathodic wave at E_p^c = -0.32 V, which gained as the scan rate was increased from 0.05 to 1.0 Vs^{-1}. The voltammetric responses remain unchanged at different scan rates, which features that initial Fe_3O_4@Au NPs are regenerated during the potential cycle. One reduction and one oxidation peaks were observed. However, the voltammogram recorded at 1.0 Vs^{-1} contained an additional weak intensity anodic wave at E_p^a = -0.84 V, which can be coupled with the cathodic wave to generate a flattened quasi-reversible redox wave **[50]** with $E_{1/2}^0$ = +0.26 V, peak separation $\Delta E = E_p^c - E_p^a = 0.52$ V and peak current ratio

$I_p^a / I_p^c = 0.47$. This is consistent with the formation of an anodic redox Au^{3+}/Au^{2+} via one electron- redox process due to ΔE value is larger than Nernstian value observed for a one electron transfer redox couple and therefore, indicates the formation of strong bonding between the Fe_3O_4@Au moieties and the electrode surface **[51, 52]**. This electro-chemical information can be correlated with the previously reported Cu^{2+}/Cu^{+}anodic redox potential data **[53, 54]**. It has been noted from **Fig. 9** that the peaks showed different layers which reflect different mass-transport mechanism at the electrodes. The curve at Fe_3O_4@Au gave a plateau shaped current which is attributed as spherical diffusion process at nanoelectrodes.

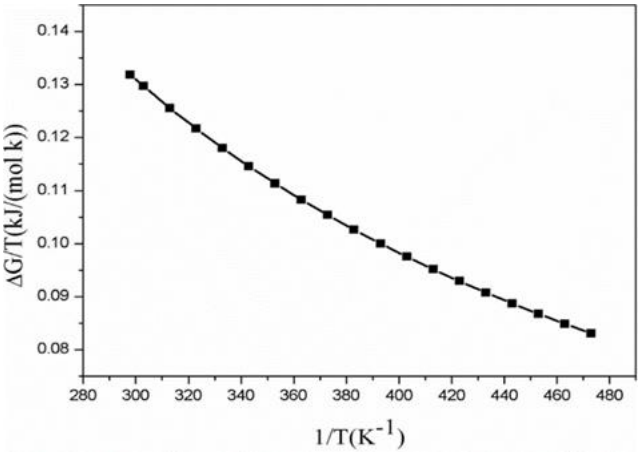

Fig. 8. Temperature dependence of Gibbs free energy obtained for Fe_3O_4@Au NPs.

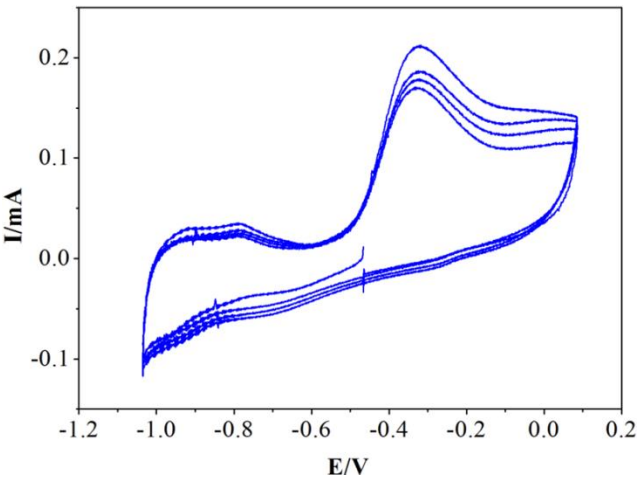

Fig. 9. Cyclic voltammogram of Fe_3O_4@Au NPs in 10^{-3} M methanol solution at 0.05, 0.1 0.2 and 0.5 Vs^{-1} scan rates.

Conclusion

In conclusion, we report the studies of electrical conductivity and thermodynamic analysis of core-shell type Fe_3O_4@Au NPs. From the analysis of results, we see that the electrical conductivity increased with an increase of temperature and the impedance showed one capacitive semicircle as well as the low-frequency-inclined spike, attributed to the grain conductivity. The Arrhenius equation was used to study the temperature dependence of electrical conductivity and the value of activation energy for Fe_3O_4@Au material was found to be 1.599 kJ/mol. Also, the thermodynamic parameters of ΔG, ΔH and ΔS were determined for the Fe_3O_4@Au material and from the analysis of these parameters, the ΔG evaluated is found positive, while the ΔH and ΔS values are negative. The negative value of ΔS indicates that the partial immobilization of ions is due to interstitial permeation and the interaction between the ion with the fixed charge groups of the material skeleton **[42]**. Our results provide experimental evidence that the material is ionic in nature due to the appearance of the spikes in the complex impedance plane plots. However, the spike towards the lower frequency range in the impedance plots is attributed to the blocking of pathway due to the ionic migration. The cyclic voltammetry study indicates the presence of quasi reversible redox couple in the solutions, as the observed peak current ratio was less than 1.0. The observed result can be attributed to one electron transfer behaviour, as the separation of anodic and cathodic peak potential with the scan rate. Interestingly, the observation of low activation energy at low temperature range is the clear evidence for the material to be acting as a suitable candidate for ion conductor and has the potential applications in many solid state devices and electrochemical sensors.

Acknowledgements

This work was supported by National Science Foundation (NSF) grants HRD0450375 (from the HBCU-RISE program) and HRD1043316 (from the HBCU-UP ACE Implementation program).

Reference

1. Mohammad, F.; Balaji, G.; Weber, A.; Uppu, R.M.; Kumar, C.S.S.R.; *J. Phys. Chem. C.* **2010**, *114*, 19194. **DOI:** 10.1021/jp105807r
2. Kumar, C.S.S.R.; Mohammad, F.; *J. Phys. Chem. Lett.* **2010**, *1*, 3141. **DOI:** 10.1021/jz101202a
3. Jacob, K.T.; Rajitha, G.; *J. Chem. Thermodyn.* **2010**, *42*, 879. **DOI:** 10.1016/j.jct.2010.02.016
4. Popov, S.G.; Levitskii, V.A.; *J. solid State Chem.* **1981**, *38*, 1. **DOI:** 10.1016/0022-4596(81)90465-5
5. Yankin, A.; Vikhreva, O.; Balakirev, V.; *J. Phys. Chem. Solids*, **1999**, *60*, 139. **DOI:** 10.1016/S0022-3697(98)00058-4
6. Wei, H.; Wang, E.; *Anal. Chem.* **2008**, *80*, 2250. **DOI:** 10.1021/ac702203f
7. Qiao, R.; Yang C.; Gao, M.; *J. Mater. Chem.* **2009**, *19*, 6274. **DOI:** 10.1039/B902394A
8. Kaushik, A.; Khan, R.; Solank, P.R.; Pandey, P.; Alam, J.; Ahmad, S.; Malhotra, B.D.; **2008**, *24*, 676. **DOI:** 10.1016/j.bios.2008.06.032
9. Huang, D.; Liao, F.; Molesa, S.; Redinger, D.; Subramanian, V.; *J. Electrochem. Soc.* **2003**, *150*, G412. **DOI:** 10.1149/1.1582466
10. Stuchinskaya, T.; Moreno, M.; Cook, M. J.; Edwards, D. R.; Russell, D. A.; *Photochem. Photobiol. Sci.* **2011**, *10*, 822. **DOI:** 10.1039/C1PP05014A
11. Brown, S. D.; Nativo, P.; Smith, J.-A.; Stirling, D.; Edwards, P. R.; Venugopal, B.; Flint, D. J.; Plumb, J. A.; Graham, D.; Wheate, N. J.; *J. Am. Chem. Soc.* **2010**, *132*, 4678. **DOI:** 10.1021/ja908117a
12. Ali, M. E.; Hashim, U.; Mustafa, S.; Che Man, Y. B.; Islam, Kh. N.; *J. Nanomater.* **2012**, *2012*, 103607. **DOI:** 10.1155/2012/103607
13. Perrault, S. D.; Chan, W. C. W.; *Proc. Nat. Acad. Sci. USA* **2010**, *107*, 11194. **DOI:** 10.1073/pnas.1001367107

14. Peng, G.; Tisch, U.; Adams, O.; Hakim, M.; Shehada, N.; Broza, Y. Y.; Billan, S.; Abdah-Bortnyak, R.; Kuten, A.; Haick, H.; *Nat. Nanotechnol.* **2009**, *4*, 669. **DOI:** 10.1038/nnano.2009.235
15. Thompson, D. T.; *Nano Today*, **2007**, *2*, 40. **DOI:** 10.1016/S1748-0132(07)70116-0
16. Huang, X.; Jain, P.K.; El-Sayed, I.H.; El-Sayed, A.; *Nanomedicine*, **2007**, *2*, 681. **DOI:** 10.2217/17435889.2.5.681
17. Cai, W.; Gao, T.; Hong, H.; Sun, J.; *Nanotechnol. Sci. Appl.* **2008**, *1*, 17. **DOI:** 10.2147/NSA.S3788
18. Glasstone, S.; Laidler, K.J.; Eyring, H.; Ed., In The theory of rate processes, McGraw-Hill, New York, 1941. **ISBN-13:** 978-0070233607
19. Arfin, T.; Yadav, N.; *J. Indus. Eng. Chem.* **2013**, *19*, 256. **DOI:** 10.1016/j.jiec.2012.08.009
20. Arfin, T.; Yadav, N.; *Anal. Bioanal. Electrochem.* **2012**, *4*, 135.
21. Harrington, D.A.; Conway, B.E.; *Electrochim. Acta*, **198**7, *32*, 1703. **DOI:** 10.1016/0013-4686(87)80005-1
22. Onwudiwe, D.C.; Arfin, T.; Strydom, C.A.; *Electrochim. Acta*, **2013**. **DOI:** 10.1016/j.electacta.2013.11.046
23. Mülazimoğlu A.D.; Yilmaz, E.; Mercimek B.; Mülazimoğlu, İ.E.; *Anal. Bioanal. Electrochem.* **2012**, *4*, 113.
24. Pournaghi-Azar, M.H.; Nahalparvari, H.; *J. Electroanal. Chem.* **2005**, *583*, 307. **DOI:** 10.1016/j.jelechem.2005.06.016
25. Kullapere, M.; Seinberg, J.-M.; Mäeorg, Maia, G.; Schiffrin, D.J.; Tammeveski, K.; *Electrochim. Acta*, **2009**, *54*, 1961. **DOI:** 10.1016/j.electacta.2008.08.054
26. Yoo, M.K.; Kim, I.Y.; Kim, E.M.; Jeong, H.J.; Lee, C.M.; Jeong, Y.Y.; Akaike, T.; Cho, C.S.; *J. Biomed. Biotechnol.* **2007**, *2007*, 94740. **DOI:** 10.1155/2007/94740
27. Chen, R.; Song, G.; Wei, Y.; *J. Phys. Chem. C*, **2010,** *114*,13409. **DOI:** 10.1021/jp912162g
28. Wang, L.; Luo, J.; Fan, Q.; Suzuki, M.; Sizuki, I.S.; Engelhard, M.H.; Lin, Y.; Kim, N.; Wang, J.Q.; Zhong, C.J.; *J. Phys. Chem. B,* **2005**, *109*, 21593. **DOI:** 10.1021/jp0543429
29. Yang, L.; Shen, Y.; Xie, A.; Zhang, B.; *J. Phys. Chem. C*, **2007**, *111*, 5300. **DOI:** 10.1021/jp067010s
30. Beg, S.; Al-Alas, A.; Al-Areqi, N.A.S.; *J. Alloys Compd.* **2010**, *504*, 413. **DOI:** 10.1016/j.jallcom.2010.05.133
31. Onwudiwe, D.C.; Arfin, T.; Strydom, C.A.; Kriek, R.J.; *Electrochim. Acta*, **2013**, *104*, 19. **DOI:** 10.1016/j.electacta.2013.04.081
32. Onwudiwe, D.C.; Arfin, T.; Strydom, C.A.; Kriek, R.J.; *Electrochim. Acta*, **2013**, *109*, 809. **DOI:** 10.1016/j.electacta.2013.07.176
33. Thangadurai, V.; Kaack, H.; Weppner, J.F.; *J. Am. Ceram. Soc.* **2003**, *86*, 437. **DOI:** 10.1111/j.1151-2916.2003.tb03318.x
34. Mackdonald, J.R.; Kenan, W.R.; Ed., Impedance Spectroscopy: Emphasizing Solid Materials and Systems, Wiley-Interscience Publication, New York, 1987. ISBN: 0471831220, 9780471831228
35. Brad, A.J.; Faulkner, L.R.; Ed., Electrochemical Methods: Fundamentals and Applications, 2nd ed., Wiley, New York, 2000. ISBN: 978-0-471-04372-0
36. Cole, K.S.; Cole, R.H.; *J. Chem. Phys.* **1941**, *9*, 341. **DOI:** 10.1063/1.1750906
37. Farea, A.M.M.; Kumar, S.; Batoo, K.M.; Yousef, A.; Lee, C.G.; Alimuddin, *J. alloys Compd.* **2008**, *464*, 361. **DOI:** 10.1016/j.jallcom.2007.09.126
38. Joubert, O.; Ganne, M.; Vannier, R.N.; Mairesse, G.; *Solid State Ionics*, **1996**, *83*, 199. **DOI:** 10.1016/0167-2738(96)00009-4
39. Barsoukov, E.; Macdonald, J.R.; Ed., In Impedance spectroscopy theory, experimental, and application, 2nd ed., John Wiley & Sons, Hoboken, New Jersey, 2005. **ISBN:** 978-0-471-64749-2
40. Arfin, T.; Rafiuddin, *Electrochim. Acta*, **2010**, *55*, 8228. **DOI:** 10.1016/j.electacta.2010.07.091
41. Arfin, T.; Rafiuddin, *Desalination* **2012**, *284*, 100. **DOI:** 10.1016/j.desal.2011.08.042
42. Arfin, T.; Rafiuddin, *J. Electroanal. Chem.* **2009**, *636*, 113. **DOI:** 10.1016/j.jelechem.2009.09.019
43. Arfin, T.; Mohammad, F.; *J. Indus. Eng. Chem.* **2013**, *19*, 2046. **DOI:** 10.1016/j.jiec.2013.03.019
44. Arfin, T.; Bushra, B.; Kriek, R.J.; *Anal. Bioanal. Electrochem.* **2013**, *5*, 206.
45. Robinson, R.A.; Stokes, R.H.; Ed., Electrolyte solutions: the measurement and interpretation of conductance, chemical potential and diffusion in solutions of simple electrolytes, 2nd ed., Butterworths Scientific Publications, London, 1959. **ASIN:** B004FBFOYW
46. Zhang, Y.Z.; Zhou, B.; Liu, Y.X.; Zhou, C.X.; Ding, X.L.; Liu, Y.; *J. Fluoresc.* **2008**, *18*, 109. **DOI:** 10.1007/s10895-007-0247-4
47. Tien, H.T.; Ting, H.P., *J. Colloid Interf. Sci.* 1968, 27, 702. **DOI:** 10.1016/0021-9797(68)90104-5
48. Ross, P.D.; Subramanian, S.; *Biochemistry*, **1981**, *20*, 3096. **DOI:** 10.1021/bi00514a017
49. Carvalho, A.E.; Alcantara, G.B.; Oliveira, S.M.; Micheletti, A.C.; Honda, N.K.; Maia, G.; *Electrochim. Acta*, **2009**, *54*, 2290. **DOI:** 10.1016/j.electacta.2008.10.035
50. Siddiqi, Z.A.; Noor, S.; Shahid, M.; Khalid, K.; *Spectrochim. Acta Part A: Mol. Biomol. Spectrosc.* **2011**, *78*, 1386. **DOI:** 10.1016/j.saa.2011.01.015
51. Salehzadeh, H.; Nematollahi, D.; Rafiee, M.; *J. Electroanal. Chem.* **2011**, *650*, 226. **DOI:** 10.1016/j.jelechem.2010.09.019
52. Zhang, N.; Zhang, X.; Zhao, Y.; *Talanta*, **2004**, *62*, 1041. **DOI:** 10.1016/j.talanta.2003.10.038
53. Selvakumar, B.; Rajendiran, V.; Maheswari, P.U.; Stoeckli-Evans, H.; Palaniandavar, M.; *J. Inorg. Biochem.* **2006**, *100*, 316. **DOI:** 10.1016/j.jinorgbio.2005.11.018
54. Hirohama, T.; Kuranuki, Y.; Ebina, E.; Sugizaki, T.; Arii, H.; Chikira, M.; Selvi, P.T.; Palaniandavar, M.; *J. Inorg. Biochem.* **2005**, *99*,1205. **DOI:** 10.1016/j.jinorgbio.2005.02.020